Ocean Wave Slope Observations Using Radar Backscatter and Laser Altimeters

D. VANDEMARK

NASA Goddard Space Flight Center, Wallops Island, Virginia

B. CHAPRON

Département d'Océanographie Spatiale, IFREMER, Plouzané, France

J. SUN

National Center for Atmospheric Research, Boulder, Colorado

G. H. CRESCENTI

NOAA Field Research Division, Idaho Falls, Idaho

H. C. GRABER

University of Miami, Miami, Florida

ABSTRACT

Combination of laser and radar aboard an aircraft is used to directly measure long gravity wave surface tilting simultaneously with nadir-viewing microwave backscatter from the sea surface. The presented dataset is extensive, encompassing varied wind conditions over coastal and open-ocean wave regimes. Laser-derived slope statistics and Ka-band (36 GHz) radar backscatter are detailed separately to document their respective variations versus near-surface wind speed. The slope statistics, measured for $\lambda > 1$–2 m, show good agreement with Cox and Munk's oil-slickened sea measurements. A notable exception is elevated distribution peakedness and an observed wind dependence in this likely proxy for nonlinear wave–wave interactions. Aircraft Ka-band radar data nearly mimic Ku-band satellite altimeter observations in their mean wind dependence. The present calibrated radar data, along with relevant observational and theoretical studies, suggest a large (-5 dB) bias in previous Ka-band results. Next, wave-diverse inland, coastal, and open-ocean observations are contrasted to show wind-independent long-wave slope variance changes of a factor of 2–3, always increasing as one heads to sea. Combined long-wave and radar data demonstrate that this long-wave tilt field variability is largely responsible for radar backscatter variations observed at a given wind speed, particularly at wind speeds below 5–7 m s^{-1}. Results are consistent with, and provide quantititative support for, recent satellite altimeter studies eliciting signatures of long-wave impacts resident in the radar backscatter. Under a quasi-optical scattering assumption, the results illustrate long-wave control on the variance of the total mean square slope parameter due to changes in the directional long-wave spectrum, with high-wavenumbers being relatively unaffected in a mean sense. However, further analysis suggests that for winds above 7 m s^{-1} the high-wavenumber subrange also varies with change in the longer wave field slope and/or energy, the short gravity wave roughness being measurably greater for smoother seas.

1. Introduction

The mean relationship between sea wave slope statistics and near-surface ocean wind speed has long been established (Cox and Munk 1956), as has the tie between these optically derived wave slope variance measure-

ments and the ocean radar backscatter measured by a microwave altimeter (Barrick 1968b; Jackson et al. 1992). However, it has also been supposed for decades that factors such as wind gustiness, currents, fetch, and long gravity wave dynamics will serve to significantly vary any such mean wind–wave correlation and its inversion using radio probing techniques (Barrick 1974). Understanding, detecting, and monitoring these dynamics using today's complement of spaceborne ocean remote sensors is a challenge requiring a blend of field measurements, modeling, and satellite data interpreta-

Corresponding author address: Douglas Vandemark, Ocean Process Analysis Laboratory, 39 College Road, 142 Morse Hall, Durham, NH 03824.
E-mail: douglas.vandemark@nasa.gov

tion. Opportunities presented include the goal to improve wind stress estimation from space by enfolding the noted second-order effects in air–sea coupling formulations at global to local scales.

Short waves with $\lambda < 10–20$ cm are considered critical to microwave remote sensing of ocean winds. This is because these wavelets respond quickly and dynamically to increases in the local wind, and because the transmit wavelength of such sensors makes the radio probing of these waves possible. However, long-wave tilting of the short waves is also fundamental perturbation carried in the increasingly common two- or three-scale models for surface wave interaction and ocean wave remote sensing alike (e.g., Bass et al. 1968; Barrick 1968a; Valenzuela 1978; Longuet-Higgins 1982; Gotwols and Thompson 1994; Liu et al. 1997; Chapron et al. 2000; Plant 2002). Such models impose a separation between long and short waves, permitting separate characterization of their wind-dependent statistics, forcing, and dissipation as well as subsequent recombination to address possible interactions between the scales. Separation is also imposed because a substantial fraction of the long gravity wave field is often due to swell and sea generated by distant or turning winds, waves that are uncoupled and misaligned as far as the local wind is concerned. Such dynamics can impact how well a remote sensor inverts wind stress and short wave information.

The following work provides new field measurements related to long and short gravity wave slopes on the sea—both their covariance with respect to local wind forcing and with longer wave dynamics divorced from the local wind. Specific goals are to document the long-wave field using directly measured slope statistics and to then to illustrate and quantify the effect that this tilting field has upon an altimeter's nadir-view normalized radar backscatter cross section, $\sigma^\circ(\theta = 0^\circ)$, and its subsequent interpretation.

When ocean altimetry is considered, aside from wind dependency, at least three factors arise in the interpretation of σ°: absolute radar calibration, long-wave impacts, and short-wave diffraction. These factors are central to σ° use in wind speed and wave spectral estimations, and in attempts to gain new geophysical insight using altimeter observations at differing transmit frequencies (Jackson et al. 1992; Elfouhaily et al. 1998). This paper concentrates mainly on the first two issues. A first-order specular point scattering theory (Barrick 1968b) is considered adequate for the examination of the first two factors:

$$\text{mss}' = \frac{|R(0^\circ)^2|}{\sigma^o(0^\circ)}, \tag{1}$$

where the numerator holds the frequency-dependent surface Fresnel reflectivity factor and mss′ is a radar-derived estimate of the surface wave slope variance, mss. One implicit assumption is that there is no a priori need to invoke an effective Fresnel coefficient in the derivation (cf. Chapron et al. 2000). This and further assumptions behind Eq. (1) are discussed in section 2d. This paper concentrates mainly on the first two issues above while the issues of diffraction and precise inference of high-wavenumber spectral information can be reviewed elsewhere (e.g., Jackson et al. 1992; Chapron and Vandemark 1996; Plant 2002).

Absolute σ° levels at the nadir view angle are addressed using a Ka-band (36 GHz) radar, in part to revisit past nadir-view Ka-band data (Masuko et al. 1986). Those data represent the only such data available at Ka-band and indicate an unexpectedly large 5–6-dB difference with respect to nadir-view X- and Ku-band observations. Recent results using an indirect absolute radar cross-section determination method (Walsh et al. 1998) suggest there may be a calibration error and this possibility will be assessed. Present results should also resemble those obtained using a satellite radar altimeter operating at 36 GHz. As such, they provide preliminary design data for proposed Ka-band altimeters such as AltiKa, a new mission being considered by the European Space Agency.

Regarding long-wave impacts, typically this gravity wave ($\lambda > 30$ cm) contribution to mss is assumed to be small $O(20\%–30\%)$ and highly correlated with wind speed; thus deviation from a nominal wind-dependent mss due to long waves is often considered unlikely or negligible. Some recent work has shown the effect should not be neglected (e.g., Hwang and Shemdin 1988; Hesany et al. 2000). Other recent satellite altimeter work (Glazman and Greysukh 1993; Hwang et al. 1998; Gommenginger et al. 2002; Gourrion et al. 2002a,b) use proxies such as significant wave height H_s to demonstrate measurable long-wave variability impacts upon σ°. Still, observed ambiguities indicate that physical explanation and quantification remains somewhat uncertain (Gourrion et al. 2002a). For example, is σ° variation strictly geometrically controlled, that is, due to long-wave tilt field changes, or is it due to perturbation of the centimeter scale waves by long-wave hydrodynamics? This study looks at such questions by considering radar σ° data collected in concert with direct measurement of slope statistics for long-to-intermediate-scale gravity waves $O(100–1$ m). These longer-wave observations are derived using a three-laser slope measurement system, providing a quantitative check of the oft-cited oil-slickened surface slope estimates reported by Cox and Munk (1956). As such, the laser results also serve the more general purpose of documenting long-wave slope statistics relevant to satellite sensors working in frequencies from L band to the visible.

The platform used to acquire the coincident wave and wind measurements for this study was the National Oceanic and Atmospheric Administration (NOAA) LongEZ research aircraft. Data were collected over a 2-yr period as part of the Office of Naval Research Shoaling Waves Experiment (SHOWEX) and the National Aeronautics

and Space Administration (NASA) Wave Profile Experiment (WAPEX). Following is an overview of the data collection, measurement techniques, and their validation. Laser-derived slope and Ka-band radar backscatter data are then presented and discussed in context of past observations. Analysis combining these tools helps to clarify, in quantitative terms, the impact of long waves on the detection of short waves and, hence, wind using remote sensors in regions such as the coastal zone.

2. Measurements and processing

Measurements to be discussed were collected over either the western Atlantic Ocean or the inland waters of Currituck Sound, always within 120 km of Duck, North Carolina. All flights occurred between 1997 and 1999, with most data collected in the month of November. Data come from 36 separate flights of the NOAA LongEZ covering a variety of wind and wave conditions. Aircraft flight patterns over the region varied to accomodate several complementary investigations (Sun et al. 2001; Vandemark et al. 2001; Mahrt et al. 2001; French et al. 2000). The composite coverage provides a dataset containing extensive sampling over open ocean, coastal, and inland water. For all data presented herein, the aircraft flew at an average altitude of 15 m above the surface. This is a unique vantage point that permits high-resolution and high-fidelity sensing of the sea surface and air above, much as for a fixed experimental platform. Efforts mentioned above describe the aircaft measurement systems and data processing used in this study; thus only details critical to this work are discussed below. All data have undergone extensive quality checks noted in the studies above. One focus here is on the wind dependence of wave slope statistics and radar backscatter. Typical time and spatial averaging windows for ocean wind measurement are 8–10 min and 5–15 km. A 5-km along-track aircraft extent is chosen for the averaging length scale in this study to retain spatial wind and wave dynamics inherent to the region (Sun et al. 2001).

a. Micrometeorology

Five-kilometer wind velocity and friction velocity (u_*) estimates are produced using the processed LongEZ (French et al. 2000) wind data and eddy covariance flux estimations (Sun et al. 2001). The main atmospheric derivative for this study is neutral-stability wind speed at 10 m above the surface, U_{10N}. Values are obtained from measured winds U_m at altitude z using

$$U_n(z) = U_m(z) + \frac{u_*\psi(z/L)}{\kappa} \quad \text{and} \quad (2)$$

$$U_{10n} = U_n(z) + \frac{u_*\log(10/z)}{\kappa}, \quad (3)$$

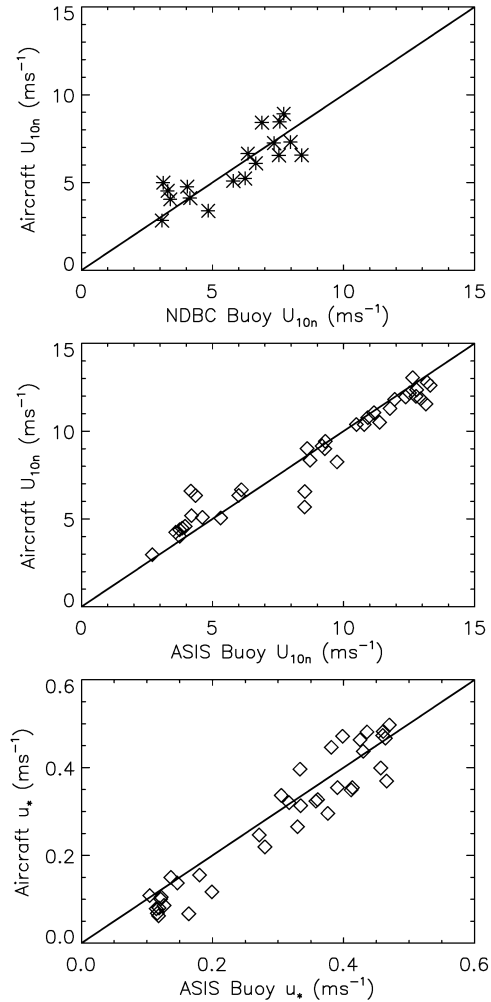where κ is von Kármán's constant; L, the Monin–

FIG. 1. Coincident near-surface wind estimates. (top) Aircraft vs NDBC bulk-derived U_{10N}, and (middle) aircraft vs ASIS eddy-correlation-derived U_{10N}. (bottom) Buoy and aircraft friction velocity estimates for the same ASIS samples shown in the middle panel.

Obukhov stability length, is computed using a bulk formulation based on Richardson's number Ri (Donelan 1974); and the stratification correction ψ follows Paulson (1970) and Dyer (1974) for unstable and stable cases, respectively. The LongEZ also measures humidity and sea and air temperature scalars needed to derive Ri. Formulation of L in terms of a bulk Ri estimate is done to avoid noise frequently introduced by the cubic u_* term needed when using direct eddy correlation estimates to derive L. While U_{10n} estimates obtained here may differ slighty from alternate methods, intercomparisons show variance to be less than 0.3 m s^{-1}, a level of accuracy that is adequate for this study.

Several in situ meteorological platforms were overflown by the aircraft during these experiments. Direct comparison of aircraft winds with those from the National Data Buoy Center (NDBC) buoy 44014, located 80 km off shore, are shown in Fig. 1. Data shown rep-

resent measurements collected within 10 km and 30 min of each other. Aircraft samples are derived from 5-km segments along the flight track, while the buoy wind is the average over an 8-min time window; U_{10n} values shown for both the aircraft and NDBC buoy are derived using the scalar quantities, including $U_m(z)$, measured by each platform. This bulk estimation facilitates comparison for this case where the buoy does not directly measure the fluxes. The Tropical Ocean–Global Atmosphere Comprehensive Ocean–Atmosphere Response Experiment bulk flux algorithm (Fairall et al. 1996) was applied to both buoy and aircraft data to derive U_{10n}. The rms difference between measures is 1.1 m s^{-1}, and close overall agreement is apparent over the available dynamic range.

A separate comparison is made using flights over the University of Miami's Air–Sea Interaction Sensor (ASIS; Graber et al. 2000) during SHOWEX in November of 1999. The maximum time and distance between surface and air measurements are 15 min and 10 km, respectively. ASIS data are derived from three separate platforms operating during SHOWEX, and all ASIS estimates, including eddy correlation fluxes, represent a 20-min averaging period. The middle panel of Fig. 1 provides intercomparison of U_{10n}, computed using eddy correlation u_* and scalar estimates from both sensors, and following Eqs. (2) and (3). The bottom panel displays ASIS versus aircraft friction velocity estimates. The linear regression correlation coefficient for both of these ASIS intercomparisons exceeds 0.94. The rms difference between U_{10n}, measures is 1.0 m s^{-1}. Overall agreement between both the flux and wind estimates in Fig. 1 indicates the aircraft wind data are well calibrated.

b. Laser altimeter system and surface slope statistics

The aircraft houses three downlooking laser altimeters, mounted to form an equilateral triangle in the horizontal plane with leg spacing of 0.96 m. This provides three simulataneous wave elevation measurements as the aircraft traverses over the surface. The sensor geometry and processing, including aircraft motion compensation, are discussed elsewhere (Sun et al. 2001; Vandemark et al. 2001). The synchronized sea elevation estimates are used to compute a surface wave slope vector at roughly 1-m-spaced horizontal intervals along the aircraft ground track. The 1-m horizontal spacing of the mounted lasers limits the wavelengths resolved to $\lambda > 2$ m. For a 5-km flight segment nominally 5000 individual slope measurements are made. The slope vector is given as $\mathbf{s} = s \cos(\alpha)\mathbf{i} + s \sin(\alpha)\mathbf{j}$, where α is the azimuthal angle with respect to north, the slope magnitude is $s = \tan\beta$, and β is the elevation angle from horizontal. The slope probability density function (pdf) for these intermediate to long-scale gravity waves is thus obtained (Vandemark et al. 1999) and the variance, skewness, and kurtosis directly computed for each data segment. Triply redundant wave elevation statistics, in-

cluding H_s (defined as 4 times elevation rms), are obtained as well. Last, a transect wavenumber spectrum can also be computed from data along a given flight track. Note that this is an encounter spectrum and, given the aircraft's nominal speed of 50 m s^{-1}, a swell or sea true wavenumber will suffer significant Doppler shifts. While not the focus of this study, transect spectra have been utilized for the case of flight legs oriented along the wind and wave direction (Melville and Matusov 2002; Sun et al. 2001). Our preliminary inspection of the high-wavenumber portion of Doppler-corrected transect spectra for varied wind conditions supports the form $k^{-3.0\pm0.1}$ down to the 2.5 rad m^{-1} cutoff in the equilibrium subrange (e.g., Banner et al. 1989). Future analysis intends to assess the level of variability for this high wavenumber subrange.

The fidelity of the laser-measured wave height and slope statistics depends upon precise compensation for the continual laser pointing angle changes due to aircraft motions. Figure 2 illustrates the quality of these corrections for the case where the aircraft performed large roll manuevers over nearly smooth inland water. Aircraft-estimated wind speed over the Currituck sound was 2.5 m s^{-1} for this data segment. After correction, results should indicate a nearly flat sea surface. Raw 50-Hz aircraft roll and laser-derived aircraft altitude, sea surface elevation, and slopes are displayed for a 2.5-km ground segment (~2500 data points). A running estimate of mss$_l$ is provided via a 200-m along-track sliding average for $\langle s_l^2 \rangle$. The computed elevation standard deviation is below 3 cm and the variance for mss$_l$ falls below 3.0×10^{-4}. Estimated H_s is 0.10 m and mss$_l$ is 1.2×10^{-3}, both indicative of a surface that is 10–30 times as smooth as typical open-ocean conditions. Results from repeated inland water legs under such manuevers are used to estimate that open-ocean rms wave height and slope uncertainties typically fall below 3%. As critical, even for these uncharacteristically large aircraft motions, wave data exhibit little correlation with that variation.

Comparison of buoy and aircraft-derived H_s measurements provides further validation. Intercomparison data are extracted from the same ASIS and NDBC data subsets discussed in the wind comparisons above. Results indicate that the standard deviation between buoy and aircraft H_s estimates falls below 0.15 m and the linear regression coefficient exceeds 0.92 over the 60 samples in the intercomparison.

c. Radar scatterometer

A Ka-band (36 GHz, $\lambda_0 = 8.3$ mm) scatterometer, pointed directly normal to the surface, is used to collect reflected power measurements from the roughened sea surface as detailed in Vandemark et al. (2001). Measured receiver voltages are converted to normalized radar cross section using the radar equation:
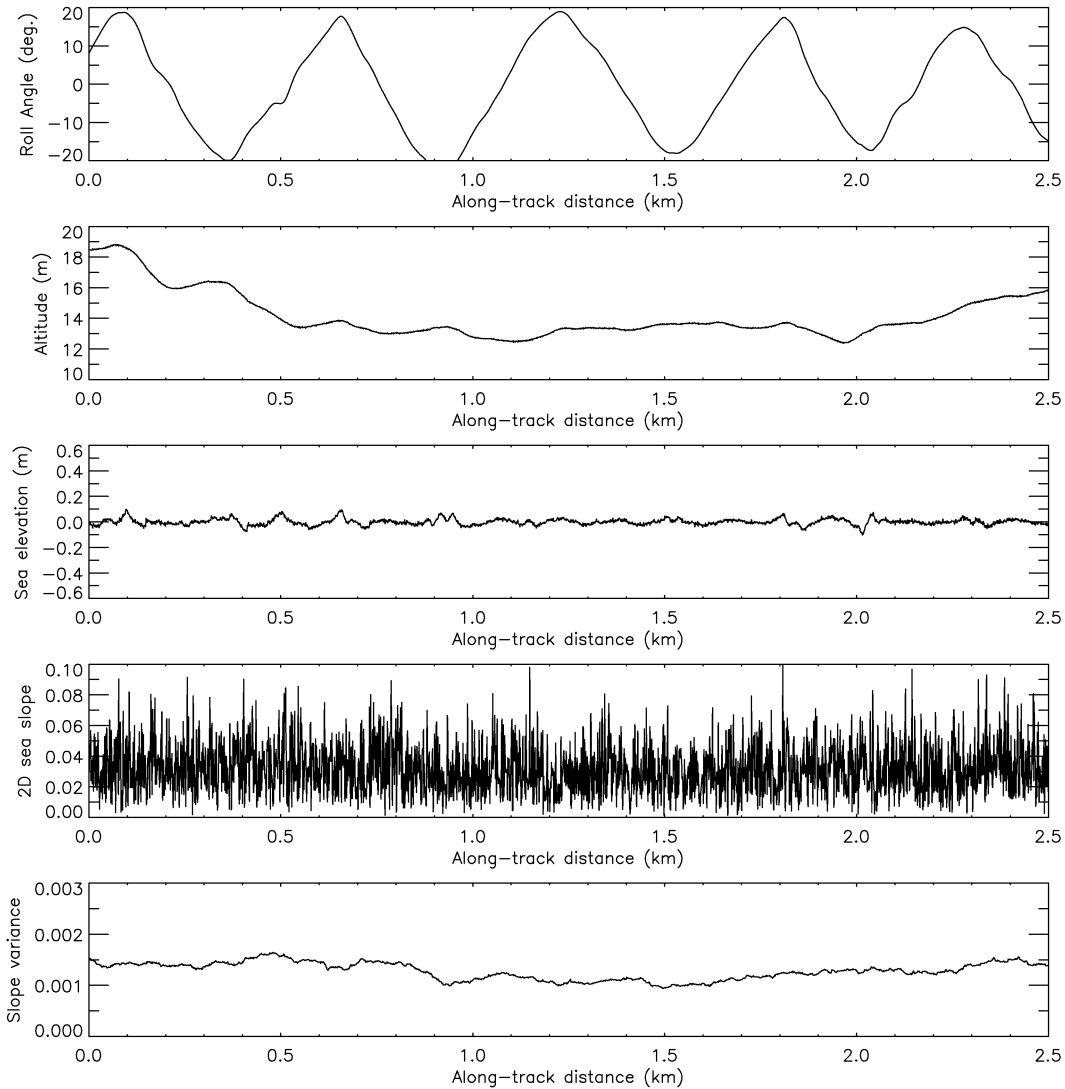
FIG. 2. Typical calibration flight leg data over nearly smooth inland water: (upper panels) aircraft roll and altitude data, (middle) the laser-derived estimate of the sea surface elevation, and (lower panels) the measured slope magnitudes s_i and variance $\langle s_i^2 \rangle$, respectively, as discussed in the text.

$$\sigma^o(0°) = \frac{P_r(4\pi)^3 r^4}{P_t G^2 \lambda_0^2 A}, \qquad (4)$$

where P_t and P_r represent the receive and transmit power levels, G the antenna gain, and λ the radar wavelength, r is the laser-derived distance from the sea to the antenna, and A is the effective observed surface area. All parameters are accurately determined and cross-checked through rigorous calibrations. Absolute calibration of the microwave system is carried out by measurement of P_r off a series of calibrated point targets before and after each measurement campaign. The radar is also equipped with an internal calibration loop, continual transmit power monitoring, and internal temperature control to better than 2°C. External calibration results indicate an uncertainty of ±0.4 dB in the absolute level. Precision for a given estimate approaches ±0.2 dB for a given 5-

km segment average in this study. This precision holds between successive campaign measurements as well as from point to point on a given day. This is a system with high horizontal resolution, having a 1-m surface footprint when flown at 10-m altitude. Data processing to provide the averaged $\sigma°$ over a given 5-km flight leg is discussed in the noted reference. The appendix describes a small $\sigma°$ correction required to adjust the wider beam antenna data collected here to that measured by a narrow-beam system such as a satellite altimeter.

d. Radar-inferred slope estimates

A common use for near-vertical-incidence radar data is the inference of the surface mean squared slope, mss. Under a geometric optics radar scattering assumption and assuming that the slope pdf conforms to a direc-

tionally uniform Gaussian form, the omnidirectional slope variance can be inverted via the inverse relationship (Barrick 1968b):

$$\sigma_{\mathrm{Ka}}^{o}(\theta) = \frac{|R(\theta)^2|}{\mathrm{mss}'_{\mathrm{Ka}}} \sec^4\theta \exp\left(-\frac{\tan^2\theta}{\mathrm{mss}'_{\mathrm{Ka}}}\right), \qquad (5)$$

where θ is the incidence angle from vertical. In this study the view angle is $\theta = 0°$, the nominal configuration for the satellite altimeter and for the present aircraft data. Thus θ dependence on the right-hand side vanishes to leave the leading fractional term, that is, Eq. (1); $\sigma°$ in this study refers to $\sigma_{\mathrm{Ka}}^{o}(0°)$. The Fresnel reflectivity factor ($|R(0°)^2|$) at Ka band is estimated to fall between 0.52 and 0.55 for the salinity and water temperatures encountered during our measurements (Stogryn 1997). This factor's 1%–3% variation is accounted for in presented $\mathrm{mss}_{\mathrm{Ka}}$ estimates based on this Stogryn model and aircraft-measured sea surface temperatures. Note that no effective Fresnel coefficient is imposed in the development. It has been traditional to invoke such a term in lieu of the true Fresnel factor to account for unexplained disagreements between observations in both the overall bias between observed $\sigma°$ and mss and in the wind dependence for these two variables (e.g., Valenzuela 1978). Chapron et al. (2000) argues that this tuning term in not necessary if one reexamines the radar and optical measurements to include the effects of slope pdf peakedness and present understanding of the absolute calibrations for Ku-band satellite datasets.

A prime notation is attached to all radar-derived mss estimates to explicitly tie these measurements to the approximations of Eq. (5). While mss′ may correlate well with an optically derived mss estimate, numerous uncertainties remain in quantitative comparisons that fall outside of this study's main objectives. These include the issues (see Jackson et al. 1992; Chapron et al. 2000; Plant 2002) of slope pdf non-Gaussianity, centimeter-scale wave steepness and diffraction of incident radiation, and wave directionality and spectral content at all scales. That said, it is asserted that Eq. (5) is adequate for the objectives at hand.

The optical scattering assumption implies the incident radiation wavelength is much shorter than all roughness lengths on the surface. For microwave probing of the ocean surface this is typically violated due to the presence of of steep gravity–capillary and capillary waves (Jackson et al. 1992). Thus, to first order, the slope variance estimate of Eq. (5) is considered as a partial integration, encompassing waves greater than $3\lambda_0$ ($k_f = k_0/3 = 250$ rad m^{-1}). This means wavelets longer than 2 cm for a Ka-band sensor.

Most important to this study is the coincident and direct measurement of the omnidirectional slope variance acquired by the lasers. This integration over the directional slope spectrum is obtained up to the laser-geometry-dictated cutoff wavenumber of $k_l \approx 3$ rad m^{-1}:

$$\mathrm{mss}_l = \int_0^{|\mathbf{k}|=k_l} |\mathbf{k}|^2 S(\mathbf{k}) \, d\mathbf{k} = \langle s_l^2 \rangle. \qquad (6)$$

This is the omnidirectional value representing slope integration over wavenumber and azimuth angle α. The wavenumber vector is $\mathbf{k} = k \cos(\alpha)\mathbf{i} + k \sin(\alpha)\mathbf{j}$. The integrand represents the slope spectral density function where $S(\mathbf{k})$ is the directional wave height spectrum. As discussed, each mss_l estimate is directly obtained over $\sim$5000 measured s_i realizations.

Therefore, the radar and laser systems provide complementary surface information over each 5-km flight interval. It is a direct step to combine measurements and infer that the short-wave portion of slope variance derived from k_l to k_f is

$$\mathrm{mss}'_h = \mathrm{mss}'_{\mathrm{Ka}} - \mathrm{mss}_l \approx \int_{k_l}^{k_f} |\mathbf{k}|^2 S(\mathbf{k}) \, d\mathbf{k}. \qquad (7)$$

The subscripts l and h are chosen to reflect the integration limits over low- and high-wavenumber portions of the spectrum respectively. Therefore mss'_h represents information on the short gravity and gravity–capillary wave contributions ($\lambda = 200$ to 2 cm). Forthcoming data interpretation makes use of mss'_h in attempts to examine the wave scales controlling observed radar backscatter.

3. Results

The mean wind dependence of surface estimates under presupposed open ocean wind and wave conditions are detailed first. Measurement locations are shown in Fig. 3. The water depth exceeds 20 m for all cases. Samples within 15 km of the coastline are excluded, as suggested by recent work on this coastline (Sun et al. 2001; Vickers et al. 2001), showing that the atmospheric boundary layer often contains strong land-induced turbulence advected 10–15 km from shore. The map also shows the location of the buoys mentioned in section 2.

This subset of aircraft data holds more than 2300 5-km samples gathered on 36 separate days over a 2-yr period. Figure 4 depicts the range and frequency of wind speeds observed along with the mean relation between H_s and the wind. The U_{10} distribution highlights that this set is weighted toward moderate wind observations, but a substantial number of high and low wind events are also present. Wave height variation with wind indicates that the sea state generally falls below 2.0 m and that, on average, H_s levels reside above a fully developed sea prediction (Sverdup and Munk 1947) for low winds and fall below this criterion for moderate to high winds. The observed levels of H_s fall well below globally observed mean values at any given wind (Gourrion et al. 2002b). This is not unexpected off this East Coast region where swell impacts are limited. All references to U_{10} from this point forward refer to the 10-m neutral stability value computed using Eq. (3).
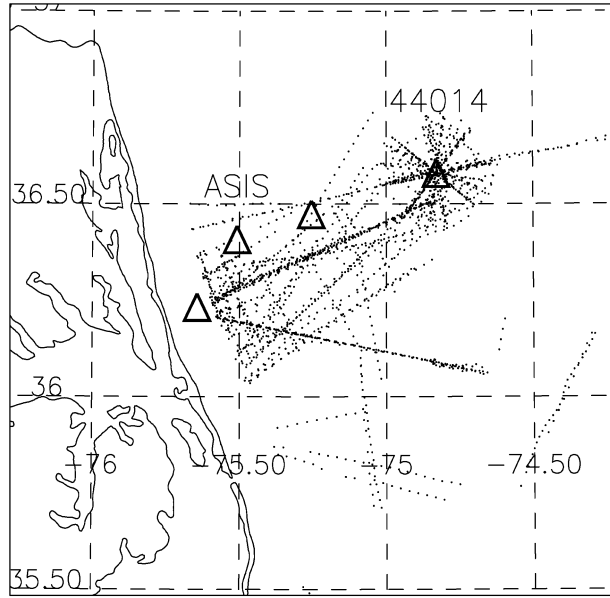
FIG. 3. The study region including a center location for all 5-km average "open ocean" aircraft data samples presented. Locations of the three ASIS buoys and and NDBC 44014 are noted. Map extent is roughly 100 km × 100 km.
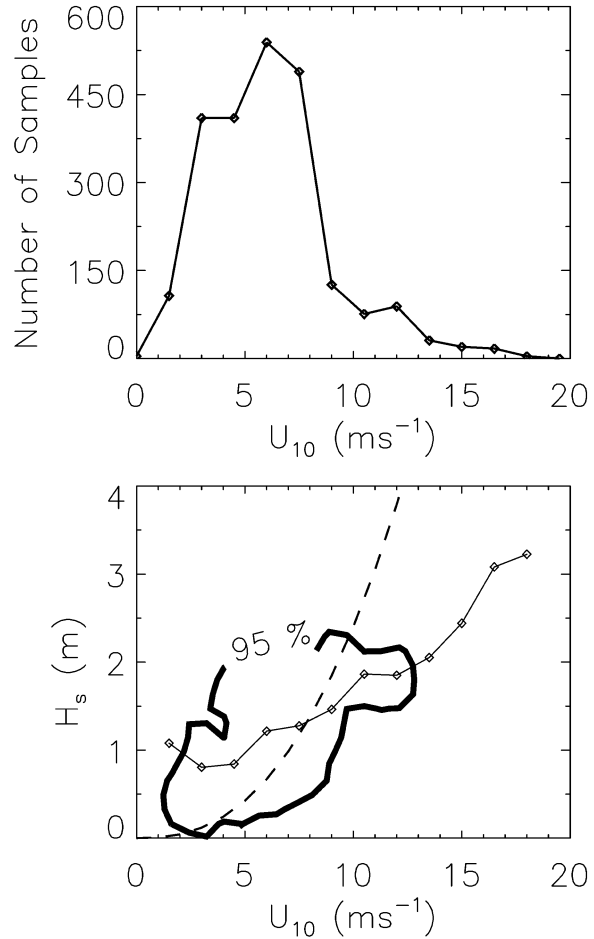

FIG. 4. (top) Histogram of wind speeds observed within the 2324 sample open-ocean dataset. (bottom) Data show the average of observed H_s vs wind speed, while the model curve represents the Sverdup–Munk fully developed sea prediction. Contour provides the 95% occurrence range for H_s over the range of observed winds.

a. Wind dependence of long gravity wave properties

Laser-derived slope amplitude statistics and their variation with wind are shown in Fig. 5. A wind-dependent bin averaging is performed for all panels, showing a parameter's mean value at a given speed ±0.75 m s^{-1}. The error bars represent 95% confidence intervals assuming a random distribution using

$$b_{\mathrm{err}} = \pm\frac{1.96\sigma_b}{\sqrt{N}},$$

where σ_b is the bin standard deviation and N is the sample number within a bin. Also shown in all panels are the optically deduced predictions (Cox and Munk 1956, hereinafter referred to as CM56). These predictions are for the special case where the surface was altered using oil to limit the presence of short waves. This so-called slick surface was considered to contain waves only greater than about 30 cm, a limit that coincides well with the 2-m limit ($k_l = 3$) of the laser geometry used here. Note that the present observations are derived from an unaltered ocean surface.

Data in the top panel of Fig. 5 provide a clear indication of wind dependence for the longer wave slope variance, mss$_l$, Eq. (6). Recalling Fig. 4, one notes that error bar magnitude follows the observed wind histogram. There is a linear trend up to 8–10 m s^{-1} that falls about 10% below the CM56 model. At higher winds, the present data fall farther below their prediction, but do indicate a continued, but weaker increase with wind. The one standard deviation levels about the mean in-

dicate 20%–30% variability, likely geophysical as discussed later.

Data also agree closely in form and magnitude with the Phillips (1977) logarithmic reinterpretation of CM56 results with $k_l = 3$ rad m^{-1}:

$$\mathrm{mss}_l = B \ln\left(\frac{k_l}{k_p}\right), \qquad (8)$$

where

$$k_p = g/U_{10}^2.$$

The curves shown represent a bounding of the observations using $B = a(1.0, 1.25, 1.5)$ and where $a = 4.6 \times 10^{-3}$ is prescribed by Phillips under the wind-driven asymptotic limit where a k^{-3} saturation subrange for the wave spectrum is established. At low U_{10} the average mss$_l$ lies considerably above zero in agreement with CM56 estimates. This suggests that, on average, the dataset carries a background wave field component at
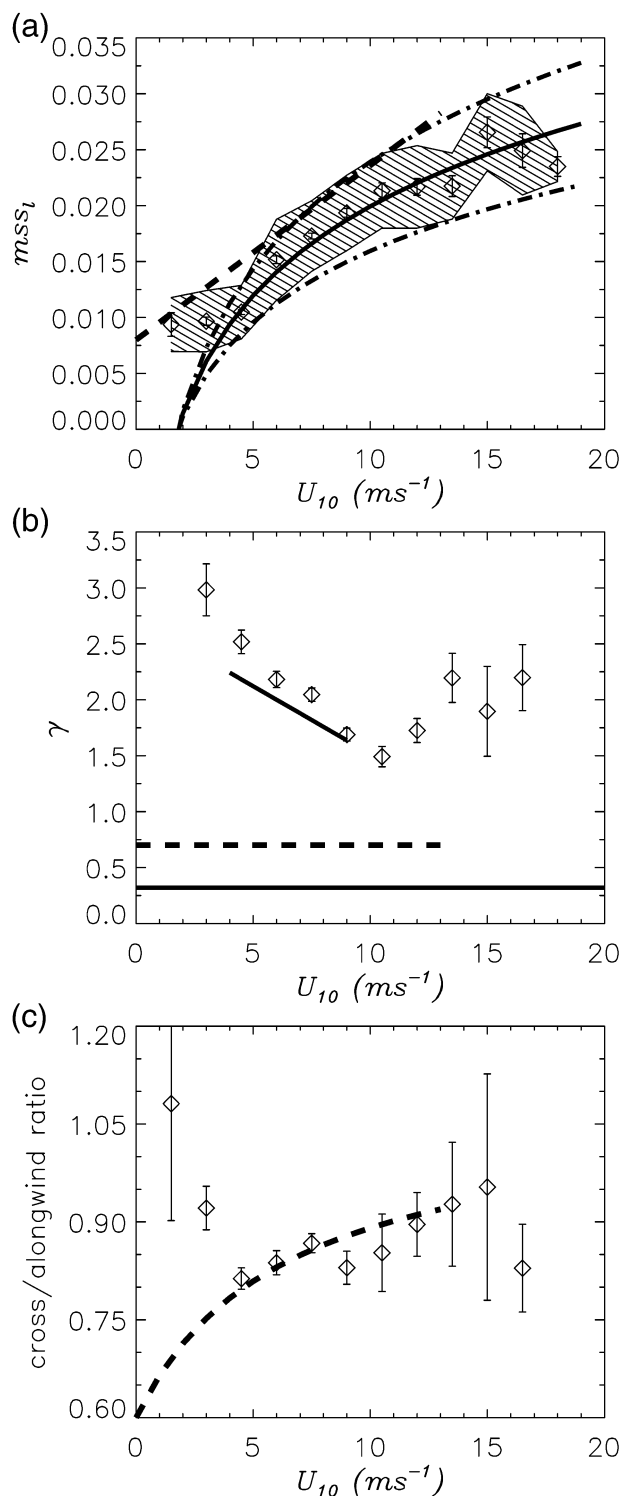
(a)

(b)

(c)

FIG. 5. Laser-derived wave slope statistics vs U_{10}. (a) The average of slope variance mss_l in successive ±0.75 m s^{-1} wind speed bins. Error bars depict the mean estimate 95% confidence interval as defined in text. The shaded region indicates $\pm$ one standard deviation for each bin. The solid and dash–dot curves are for the Phillips logarithmic model as discussed in the text. (b) The kurtosis excess coefficient γ, where the uppermost curve is derived from Shaw and Churnside (1997) and the lowest line gives γ for the Rayleigh dis-

light winds that elevates mss_l slightly above a solely wind-dependent level.

Wind-dependent kurtosis estimates, also derived from the two-dimensional slope amplitude measurements, are shown in Fig. 5b. The kurtosis excess coefficient γ is defined as

$$\gamma \equiv \frac{\mu_4}{\mu_2^2} - 3, \qquad (9)$$

where μ_i is the ith central moment of the univariate slope distribution. By definition, γ is zero for the normal distribution. The positive-definite omnidirectional slope distribution for normally distributed slopes is the Rayleigh distribution for which $\gamma = 0.245$. Data in Fig. 5b show that γ always lies well above the Rayleigh value, indicating an excess in steep and shallow slopes. The measured peakedness is largest for lightest wind and there is a clear decrease with increasing wind up to 10 m s^{-1}. Above this speed the magnitude rises again. CM56 also inferred non-Gaussian γ levels, but their technique's fidelity in resolving steep waves and the resulting observations provided no evidence of wind dependence. The γ level presented for CM56 is derived from their principal component Gram–Charlier slope fit parameters, C_{40} and C_{04}, and our subsequent omnidirectional simulation relating component slope statistics to those computed over the modulus $|\mathbf{s}|$. That simulation is based on the pdf generating function discussed in the appendix. Results indicate that CM56's $\gamma = 0.70 \pm 0.35$. CM56 also reported that this peakedness magnitude did not change substantially between the slick and clean surface observations.

While their γ estimate is included here, it is important to note that the CM56 technique involved indirect inferrence of the variance, skewness, and kurtosis under given assumptions and limitations. This included an inability to measure the true slope variance and the steepest waves, and truncation of their Gram–Charlier fit to fourth order. These are points specific to the CM56 study that should be considered in quantitative definition and use of the slope distribution (Tatarskii 2003; Chapron et al. 2000). In this case, the CM56 γ is given as reference but it is suggested that the uncertainty and mean level may exceed what is derived from their truncated fit coefficients.

A similar γ adjustment from one to two dimensions is applied to the wind-dependent findings of Shaw and Churnside [1997, their Eq. (17)]. The resulting fit is shown in Fig. 5b. In all cases, the present data and those of Shaw and Churnside (1997) lie above CM56. Close agreement in magnitude and wind dependence is observed between present data and Shaw and Churnside

tribution. (c) The ratio of cross- to alongwind mss_l. The dashed lines in all panels correspond to Cox and Munk (1956) predictions based on oil-slickened surface observations.

(1997). The latter results come from an optically based field study where the slope pdf was deduced over all wave scales, thus including wavelengths much shorter than those measured here. That study also involved a technique with angular resolution that far exceeded the CM56 study and permitted a Gram–Charlier expansion truncated at the eighth order.

Figure 5c provides the average estimate of the ratio between crosswind and alongwind slope variances obtained for these longer wave scales. Almost no asymmetry is observed for the lowest wind speed, but with much uncertainty. Otherwise, the data lie between 0.8 and 0.9, indicating weak asymmetry that varies little as the wind increases. No clear wind dependence emerges considering the given uncertainties. The CM56 surface slick model shows close agreement with the present results for winds above 5 m s^{-1}.

Last, computed slope skewness values (not shown) are small for both along- and crosswind estimates, never exceeding -0.1, where negative values assign the most likely slope as falling to the downwind side of the pdf. The mean value for both falls at -0.01 ± 0.20 and uncertainty is too high to assign significance to a small observed magnitude increase with wind seen in the alongwind measure. These findings are also consistent with that observed in CM56.

b. Wind dependence of Ka-band $\sigma°$

Nadir-view radar backscatter versus U_{10} is shown in Fig. 6. As above, the data correspond to the open ocean sample locations shown in Fig. 3 and comprise more than 2000 observations. Figure 6a presents the individual measurements as well as the other available data for this frequency and viewing geometry as obtained by Masuko et al. (1986). There is a large difference between these two studies where the present data consistently lie 5 dB above the Masuko dataset.

Referring solely to the present dataset it is pointed out that the data generally fall ±1 dB about the mean bin-averaged result with a somewhat larger data spread occuring at moderate U_{10} where more observations and, hence, diverse weather patterns were sampled. While this study is primarily focused on the ensemble dependencies, one group of outlying data are noted. The samples having $\sigma° = 10$–11 dB and winds from 6 to 10 m s^{-1} were examined and found to represent data from three days where the swell was opposed to the wind direction and/or a cold-air outbreak was in progress over the coast. Such distinctions are being addressed in a paper to follow and are mentioned primarily to highlight the point that data variability observed in Fig. 6a is foremost physically driven rather than measurement noise.

The bin-averaged $\sigma°_{Ka}$ result shown in Fig. 6a is repeated in Fig. 6b with the addition of b_{err} to delimit the estimate confidence interval. This result is then adjusted slightly downward at each wind bin based on the an-
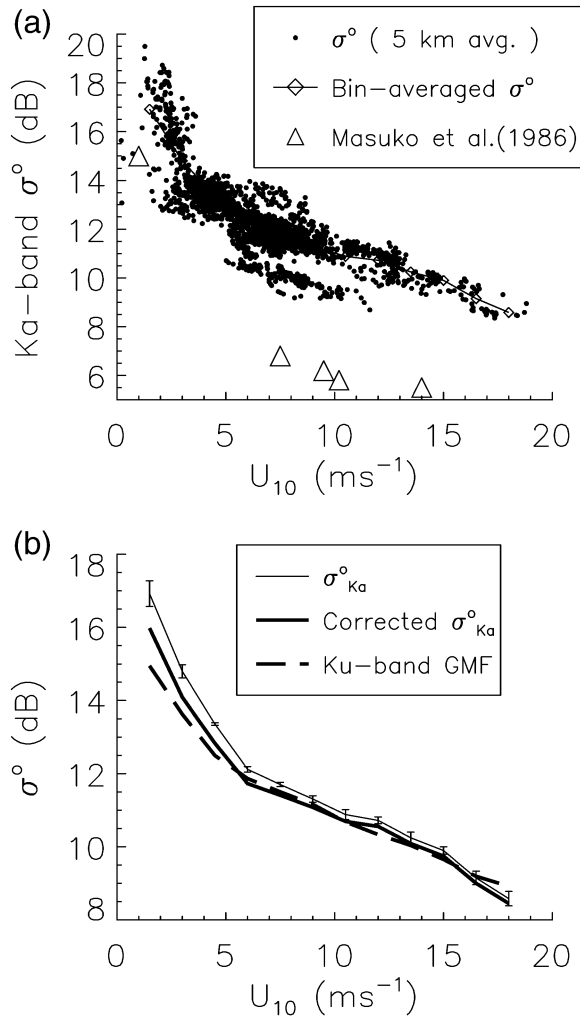

FIG. 6. Measured nadir-view $\sigma°_{Ka}$ vs U_{10}. (a) Individual data are shown along with the bin-averaged results as in Fig. 5, and Ka-band measurements ($\triangle$) from Masuko et al. (1986). (b) The aircraft bin-averaged results of (a), results after correction according to the appendix, and a Ku-band prediction based on global TOPEX altimeter observations.

tenna pattern correction model discussed in the appendix. The adjusted result provides an improved estimate of $\sigma°_{Ka}(0°)$ for direct comparison with results using narrow-beam antennas. One such result is provided on Fig. 6b as $\sigma°_{Ku}(0°)$ versus U_{10} derived from an extensively validated Ocean Topography Experiment (TOPEX) satellite altimeter–derived model at Ku band [Gourrion et al. 2002b; Eqs. (3)–(7)] given as

$$\sigma°_{Ku}(0°) = f(U_{10}, H_s). \qquad (10)$$

Here, all aircraft measures of H_s for a given wind bin are fed into Eq. (10) and averaged to produce the Ku-band geophysical model function (GMF) curve shown. Model-predicted $\sigma°_{Ku}(0°)$ depends foremost upon U_{10} but the added influence of H_s data gained through Eq. (10) should serve to adjust globally derived $\sigma°_{Ku}(0°)$ results
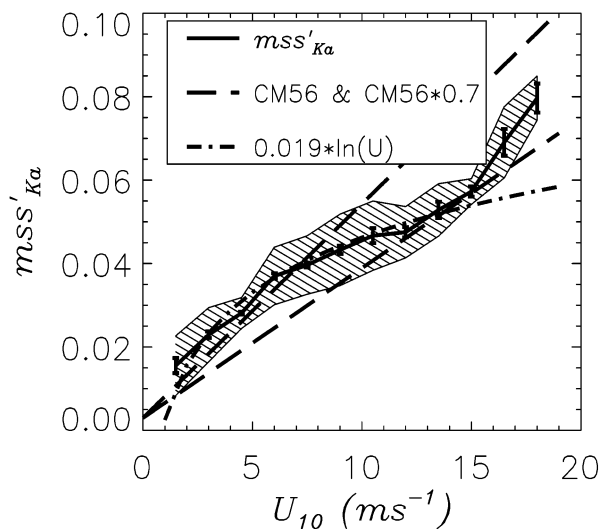
FIG. 7. Slope variance inferred from σ°_{Ka} and bin-averaged vs U_{10}. Error bars and shaded region follow the convention of Fig. 5a. Dashed lines correspond to the CM56 prediction for a clean surface and 70% of that prediction. The curve is a logarithmic fit to the present data.

FIG. 8. Locations of all individual inland (larger symbols) and coastal aircraft measurements. Map extent is roughly 100 km × 50 km.

toward the specific H_s wave climate carried in the present aircraft dataset (see Fig. 4).

Comparison of the wind-dependence between Ku-band and Ka-band observations in Fig. 6b indicates close agreement. Below winds of 5 m s^{-1} the Ku-band results fall below those at Ka band by 1 dB at most; otherwise the data agree to within ±0.2 dB for winds of 5–15 m s^{-1}. According to Eq. (1), holding mss′ constant, Ka-band and Ku-band (14 GHz) results should differ by the ratio of their Fresnel coefficents (~0.6 dB) where the Ka-band should fall below the Ku-band data. While the predicted −0.6 dB offset for Ka band is not consistently observed, absolute calibration of either system to a level better than ±0.5 dB is understood to be unlikely. This suggests that Ka-band σ° levels are consistent with prediction based upon a quasi-optical assumption and sensor calibration limitations. Thus results to consider here are that the Ka-band data agree closely with the Ku-band results in their magnitude and mean wind-dependent characteristics and that the magnitude of $\sigma^\circ_{Ka}(0^\circ)$ data cited in Masuko et al. (1986) should be regarded with caution.

Next, $\sigma^\circ_{Ka}(0^\circ)$ data are converted to a slope variance parameter, mss′$_{Ka}$, as discussed in section 2 with results shown in Fig. 7. To give a sense of the overall supposedly geophysical scatter, the standard deviation for a given wind bin is also depicted. As is common, mss′$_{Ka}$ is compared here with the optically derived clean surface model of CM56, and one sees that the radar-derived results follow that model at light winds and tend toward a 70%–80% fraction of the prediction at moderate to high U_{10}. The present data follow a logarithmic fit quite well from 1 to 15 m s^{-1}, having the form mss′$_{Ka}$ = 0.019 ln(U_{10}).
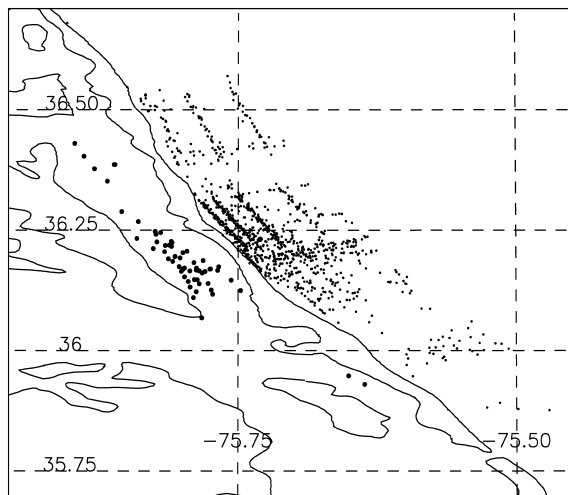
Jackson et al. (1992), among others, provide exten-

sive comparison between radar and optically derived mss estimates. The close agreement observed between present Ka-band and TOPEX altimeter Ku-band results suggests these new mss′$_{Ka}$ estimates will follow that work, at least as far as mean wind dependence is concerned. One notable point in that regard is that the present data are derived directly from absolute nadir-view σ° as for the satellite altimeter, whereas much of the recent aircraft work uses an alternate approach (e.g., Jackson et al. 1992; Walsh et al. 1998; Vandemark et al. 1997; Hesany et al. 2000) where the σ° variation with θ is measured. One then estimates mss′ via Eq. (5).

c. Long gravity wave impacts

A point to recall is that this dataset, while regionally limited, is extensive in its sampling at wind speeds below 12 m s^{-1}. Flight data were acquired under differing synoptic conditions and in this section the observed variability in aircraft wave estimates at fixed wind speeds is examined. A main objective here is to quantify the extent of wind-independent long gravity wave variations and their impacts upon σ°, and equivalently on mss′$_{Ka}$. As a first illustration, consider a spatial partitioning of the dataset into inland, coastal, and open-ocean observation subsets. Figure 8 depicts sample locations for the former two cases while Fig. 3 provides the latter. Both mss$_l$ and mss′$_{Ka}$ estimates are averaged versus U_{10} for each of these zones and the results given in Fig. 9. No wind bin holds fewer than five estimates. Note that the inland water was sampled less often than for the other cases. The unique perspective provided by the aircraft shows that for a fixed wind there is a clear overall increase in the roughness measured by both the radar and laser systems as one progresses from the sheltered to
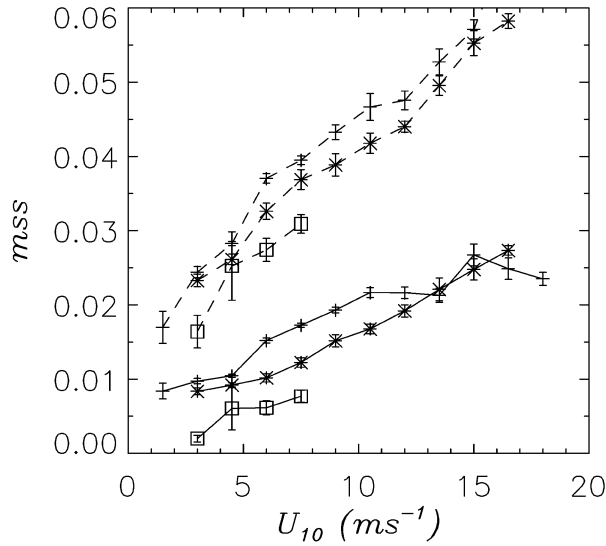
FIG. 9. Laser- and radar-derived mss vs U_{10} for the prescribed inland ($\square$), coastal (*), and open-ocean (+) regions. The lower three curves represent mss_l, the upper curves mss'_{Ka}. Error bars depict b_{err} as defined in text.

FIG. 10. Inferred short-wave term mss'_h vs U_{10} for the prescribed inland ($\square$), coastal (*), and open-ocean (+) regions. The dashed curve represents Eq. (11), a fit through these data.

open waters. Results hold for $U_{10} = 3$–12 m s^{-1} in a fairly consistent quantitative manner where a factor of 2–3 increase in mss_l is observed from inland to open waters. Note that this average result represents the ensemble over varied on-, off-, and alongshore wind and wave situations, yet the general smooth-to-rough picture always holds across the inland-to-open sea transition. Changes in mss'_{Ka} follow the same trends but are smaller, $O(20\%-50\%)$.

The observed magnitudes in mss variation indicate that $\int k^2 S(k)\,dk$ varies significantly from shore to sea. The partitioning chosen here is perhaps less physically attractive than data division by other wave field descriptors such as wave age, fetch, or sea versus swell content. A depiction of the long-wave control on the overall slope variance (mss'_{Ka}) does emerge. Using Eq. (7), mss'_h results of Fig. 10 show the retrieved high-wavenumber information for these disparate wave zones. It is evident that the data collapse onto a single wind-dependent curve, closely approximated as

$$mss'_h(U_{10}) = 0.004 + 0.0093 \ln(U_{10}), \quad (11)$$

and that all estimates agree to within 5% over the range from 3 to 12 m s^{-1}. As with mss'_{Ka}, a logarithmic form in U_{10} holds for mss'_h, indicating a change in sensitivity at a speed of ~ 7 m s^{-1}. The wind-generated short waves appear to adhere to the same form over the diverse range of longer gravity wave tilting conditions. The overall convergence of the data suggests that, in an average sense, most sea-to-shore mss'_{Ka} variability observed in Fig. 9 is due to long-wave scales, that is, those with λ exceeding the laser system's 2-m cutoff.

Results of Fig. 10 raise the question of whether the observed high-wavenumber signature is indeed solely
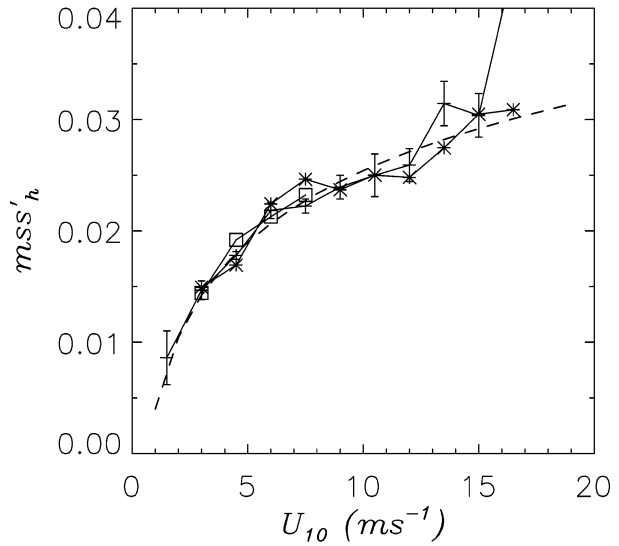
dependent on U_{10}. One means to assess this question is to stratify $mss'_h(U_{10})$ against the long-wave slope variance. Results for two disparate mss_l levels are provided in Fig. 11. Here data from both coastal ocean and open-ocean sampling were included in the averages to improve the statistical confidence. Estimated means do not differ substantially from those obtained using only the open-ocean data.

Recall that the mss_l estimator represents an azimuthally and spectrally integrated parameter and therefore serves as an average for the overall gravity wave steep-
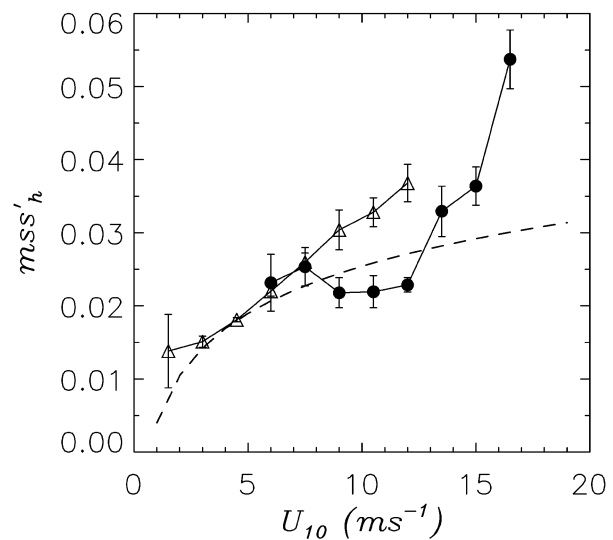

FIG. 11. Inferred short-wave term mss'_h vs U_{10} for the ensemble over estimates having $mss_l = 0.012 \pm 2.0 \times 10^{-3}$ ($\triangle$) and $mss_l = 0.024 \pm 2.0 \times 10^{-3}$ ($\bullet$). The dashed curve represents the fit given by Eq. (11). Estimates include both open- and coastal ocean observations.

ness, albeit weighted toward shorter gravity waves. Referral to Fig. 9 indicates that the low and high mss_l values chosen for Fig. 11 represent nominal levels for light to moderate and high winds, respectively. Figure 11 mss_h' estimates for these mss_l levels indicate close agreement at winds of 5–7 m s^{-1} but a systematic difference above this velocity. The short-wave roughness is higher for the smoother long-wave level, $mss_l = 0.012$. The difference holds for U_{10} of 7–13 m s^{-1}. Above this point, sampling at the low mss_l level is not available. At the higher winds, these observations can be considered to contrast mss_h' for the case of smooth seas, where the wave field is underdeveloped (the low mss_l level), with the case of fully developed and/or a mix of sea and swell (the high mss_l level). Under this rendering one sees as much as a 60% mss_h' roughness increase for the smooth seas relative to the rough. Results clearly indicate that for winds above 7 m s^{-1} this short-wave signal can vary systematically with the wave field independent of the mean wind speed. An additional check of this behavior is obtained by replacing mss_l with H_s in reproduction of Fig. 11. Results are not shown but they provide the same qualitative picture, lower H_s correlates with increased mss_h'.

4. Discussion

The laser-derived slope data of section 3 provide field measurements having several key features. First, the fidelity of direct slope measurements is likely to be superior to optical glint deduction, and to the ill-suited approach of inferring higher-order wave slope statistics via temporal buoy-based acceleration data under a quasi-linear dispersion model. Moreover, these measurements do not require oil dampening to artificially impose k_l. Last, the extensive dataset provides a robust new source for intercomparison with the nine independent slick surface realizations of CM56 that have long served as a baseline for numerous wind–wave, air–sea interaction, and remote sensing modeling efforts.

In an overall sense, the accord with CM56 results seen in Fig. 5 is impressive. As one expects, the present mss_l data fall slightly below CM56, in line with the estimation that k_l was 20 for that study as compared with 3 here. Qualitatively, the data above $U_{10} = 3$ m s^{-1} provide further support for a logarithmic, rather than linear, mss_l dependence upon wind. For a quantitative fit to the data we use the saturation subrange form of Phillips (1977) where the model is scaled solely by the wind-independent coefficient in Eq. (8). Figure 5a shows that $B = 5.7 \times 10^{-3} \pm 25\%$ spans the $\pm\sigma$ for the observations. Note that the upper bound nearly matches the CM56 result where k_l is 6 times as high. This point suggests the uncertainty resident in estimating mss_l wind dependence based on limited field observations. As a further point, the present mean results are derived over an ensemble that includes few, if any, classical fully developed sea cases. It is more typical to
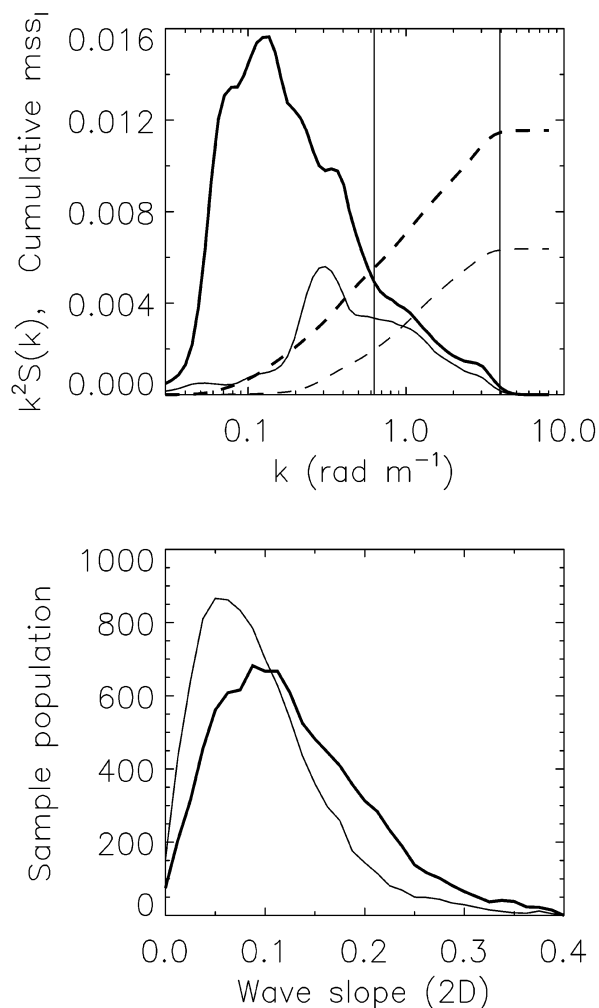

FIG. 12. Measured wave slope data for two separate cases in which $U_{10} = 8$ m s^{-1}. Thick curves represent the case of $H_s = 2.1$ m and $mss_l = 0.024$. Thin curves are for $H_s = 0.8$ m and $mss_l = 0.014$. (top) Alongwind (x axis) transect slope spectra $[k_x^2 S(k_x)]$ and cumulative mss_l estimates (dashed curves) as derived from a single laser's wave elevation estimates along the flight track. Vertical lines are high-wavenumber cutoff values for typical buoy or wave model data (to the left) and the present aircraft data (right). (bottom) Corresponding laser-derived omnidirectional slope probability density functions.

find in this data a mix of over- and underdeveloped vantage points with the seas either decaying or building. The Phillips form estimates mss_l assuming that the total is derived only from wave scales having $k < k_p$; the peak wavenumber for a fully developed sea. Thus, at least at moderate winds, one might suppose that the central value for B represents the fully developed sea while the upper limit tends to a mixture of sea and swell and the lower limit toward that of young or dying seas. The supposition is more tenuous at winds above 10 m s^{-1} where H_s levels in the present dataset indicate that observations were generally for young seas. Thus a fully developed estimate likely tends toward the upper bound. These issues are addressed further in Fig. 12 to be dis-

cussed shortly. Note that use of an equilibrium model (e.g., Banner 1990) in lieu of the saturation subrange assumption leads to similar qualitative interpretation.

Regarding other gravity wave slope statistics, data here agree with the findings of CM56 regarding minimal slope skewness and an observed cross-to-alongwind slope variance ratio of about 0.85, both parameters varying little with change in the wind. Distribution peakedness levels in Fig. 5b also affirm the long-wave slope pdf nonlinearity deduced by CM56. Present observed levels are measurably higher than for CM56 and depict a wind dependence not seen in that data. These differences are likely a result of the higher fidelity in the present direct slope measurement approach. What do the differences tell us? First, that gravity wave nonlinearity is a fundamental feature in the long-wave slope pdf and is perhaps greater than supposed. Theoretically, under a narrowband dominant wave framework, kurtosis excess in the wave slope pdf is indicative of third-order nonlinear wave–wave interactions (Longuet-Higgins 1963) whereby a correlation between the dominant long-wave and short-scale gravity waves exists. This nonzero correlation is evidenced by the increased occurence of steep wavelets near the long-wave crests and flattened areas within the troughs. These interactions also act to drive directional uniformity at the short scale, consistent with the low observed difference between the along and crosswind mss_l. While no generalized theoretical model exists for depicting these nonlinearities over all of $S(k)$, recent study of the non-Gaussian slope pdf (e.g., Liu et al. 1997; Chapron et al. 2000) suggests that γ may be empirically related to the wave spectral bandwidth parameter and to the inherent compounding of nearly Gaussian processes at multiple gravity wave scales. The wind dependence observed in Fig. 5b is consistent with a dependence on wave–wave interactions. These interactions can become predominant in the low wind, low mean slope environment where wave groupiness and multimodel wave fields can force local peakedness in the absence of wind. As wind levels increases, the data indicate γ tends toward a local minimum suggesting the most linearized situation comes at moderate winds, while as the wind increases past 10 m s^{-1} it may be that the weight toward young seas within this dataset provides enough active wave breaking to increase the level of wave steepening once again. Strong directionality of the intermediate-scale gravity waves may also play a role in explaining observed γ values, especially at light winds. In this case even weakly non-Gaussian slope distributions in the along- and crosswind directions can lead to a strongly peaked 2D distribution. While not shown, a picture similar to that of Fig. 5b emerges if one replaces U_{10} with mss_l.

Section 3c provides a view of diverse wave climates and slope pdf dynamics for various fixed wind speeds. Figure 9 illustrates the mss_l variability encountered as one spans inland, coastal, and open water. The obvious extreme of inland water, obtained over the shallow

(depth < 5 m) Currituck Sound, provides data with no swell and limited seas, along with requisite wave dissipation. In this case, one sees mss_l tends to very low levels at light wind and a factor of 3 below the open ocean at the moderate speed of 7 m s^{-1}. While not shown, the levels of slope peakedness are also reduced consistent with the expected reduction in nonlinear wave–wave interactions. A more in-depth look at mss_l variations within the coastal zone can be found in Sun et al. (2001).

Overall, mss_l variability for a fixed U_{10} is not small and likely warrants consideration in modeling and inversion studies related to remote sensing of waves and wind near the coast. This is particularly true for sensors most sensitive to the lower wavenumbers such as the low-incidence angle radar scatterometers, altimeters, and envisioned L-band systems for sensing ocean salinity and wind.

The ad hoc wave zone partitioning used to generate Fig. 9 is one means to elicit tilt field variability. To further illustrate this variability at a fixed wind speed, results from two open-ocean aircraft data collection segments are contrasted in Fig. 12. The flight transects were 5 km long and flown in the alongwind direction in both cases. Transect wavenumber spectra (1D) and slope pdf (2D) data are provided. The pdf results for the slope magnitude are derived from the individual facet slopes as discussed in section 2. Each transect (one-dimensional) slope spectrum comes from an encounter wave height–wavenumber spectrum [$S(k_x)$] computed using the along-track wave elevation spatial series data [$\eta(x)$] collected using one of the aircraft's laser altimeters. The cumulants displayed represent the alongwind variances $\langle s_x^2 \rangle$.

The low slope ($mss_l = 0.014$) case represents a young sea plus old swell case while the higher slope ($mss_l = 0.024$) example is one of a developed sea and swell; H_s is 0.8 m for the former and 2.1 for the latter. Clearly, for these 8 m s^{-1} wind speed cases the overall surface tilt fields differ substantially. The 2D pdf results show the substantial discrepancy between surface steepness for the two cases. Recall that these are slope measurements derived across a 1-m facet scale. The spectrally resolved data for alongwind flight legs, including cumulative alongwind mss_l estimates, provide a sense of the wave scales dictating mss_l. For example, there is measurable swell energy present for the low slope case at $k = 0.05$ rad m^{-1}, but its magnitude in the slope spectrum and upon the mss_l estimate is negligible. What drives the large difference between these two realizations are wave scales from $k = 0.2$ to 1 rad m^{-1}. Within the equilibrium subrange from $k = 1$–3 rad m^{-1} the differences are smaller and the contributions to mss_l similar.

The control of mss_l variability by relatively low wavenumbers suggests that operational wave buoy data may serve to examine and bound the extent of wind-independent mss_l variation. The nominal cutoff wavenumber

for NDBC wave buoy directional wave measurements is provided on Fig. 12. This implies that a substantial fraction (~30%–50%) of the example mss_l could be inferred via the measured buoy acceleration variance. Indeed, multiyear climatologies of buoy-derived mean squared acceleration for regions such as the Great Lakes, Hawaii, and the U.S. West Coast (Gourrion et al. 2002a) suggest a dynamic range in this longer wave slope variance of ±60%–80%, not unlike that observed in the mss_l results of Fig. 9.

Discussion of the presented radar backscatter data can be couched in terms of (i) examining multifrequency σ° observations, (ii) long-wave effects on altimeter backscatter, and (iii) the radar inference of surface wave information.

(i) First, regarding multifrequency observations of σ°, the present radar measurements were undertaken in part to reproduce past nadir-view Ka-band data (Masuko et al. 1986). While only a small sampling, those past results indicate a large difference between reported X- and Ka-band σ° estimates that lies far outside that predicted solely based upon the 0.6-dB difference between respective Fresnel reflection coefficients. Several studies (e.g., Jackson et al. 1992; Walsh et al. 1998) suggest those Ka-band data are much too low in an absolute sense, and inconsistent with what is known from other radar observations (e.g., Jackson et al. 1992; Chapron et al. 2000) and from optically derived slope spectral density data at high wavenumbers, while others (e.g., Apel 1994) make use of the Masuko data to infer an accordingly increased slope spectral density at these wave scales. The new data of Fig. 6a show a large 5-dB discrepancy that supports the former view. Section 3 results also show the present data to be consistent with satellite observations at Ku-band to within the error of $O(1 \text{ dB})$ system calibrations. Results are also consistent with the calibrated Ku-band tower data of (Melville et al. 1991). Last, it is noted that the Masuko et al. (1986) data were obtained by averaging of log amplifier outputs. This would serve to bias both their X- and Ka-band estimates by 2–3 dB. However, this would not alter their observed 5-dB difference between frequencies. We conclude that the present Ka-band results are a preferred choice for physically based interpretations and for spaceborne sensor signal-to-noise design considerations.

The wind dependence of open-ocean aircraft Ka-band results are shown to nearly replicate the Ku-band TOPEX altimeter model function (Gourrion et al. 2002b) in Fig. 6b. This agreement between a globally derived satellite result and data from off U.S. East Coast suggests a robust mean relationship between wind and $\sigma^\circ(0^\circ)$ consistent with numerous past aircraft studies (e.g., Jackson et al. 1992; Vandemark et al. 1997; Hesany et al. 2000; Chen et al. 2001). Certainly these aircraft data closely emulate Ku-band altimeter backscatter characteristics in a mean sense that suggests their utility for supporting satellite data interpretation.

The close agreement at all U_{10} between the Ka- and Ku-band systems is not completely in agreement with that found between C- and Ku-band σ° using systems aboard the TOPEX satellite (Elfouhaily et al. 1998). In that study a wind-dependent C-Ku band σ° difference is observed for moderate to high U_{10}, increasing with U_{10} from 0.1 to 1.0 dB. This trend is attributed to increase in short-wave spectral content following optically derived results on the increase in wave density at high wavenumbers with U_{10} (Hwang et al. 1996; Elfouhaily et al. 1997). This logic predicts the mean difference between Ka- and Ku-band σ° data should exhibit a similar wind dependence but with a slightly reduced magnitude. This study does not contain the coincident Ku- and Ka-band data needed to examine this small difference signal. The aircraft versus satellite model results of Fig. 6b show no clear wind-dependent depression of σ° at Ka with respect to Ku band like that seen for C and Ku band. Given the small expected signal we consider the results inconclusive. At best they suggest wind-dependent change between nadir-view σ° at radar λ_0 of 2.1 and 0.83 cm is small. One consistency between Elfouhaily et al. (1998) and this study is seen in their Fig. 2c and the present study's Fig. 11 where both observations indicate long-wave field control on short waves as discussed below. One inconsistency is that we see no large 3-dB frequency-dependent (Ku-to-Ka) offset like that observed between C and Ku band for the TOPEX altimeter (Elfouhaily et al. 1998). It is our contention that the wind-independent 3-dB TOPEX bias is largely due to calibration error (Chapron et al. 2000). Regardless, absolute calibration for the satellite altimeter C-band systems (TOPEX and *Jason-1*) is not performed at a level sufficient to achieve scientific certainty beyond the 1–2 dB. Accurately calibrated data are needed to fully resolve this issue.

(ii) Coincident observation of σ°_{Ka} and mss_l in this dataset provides a unique perspective for assessing the impact of tilt field variability upon altimeter backscatter. It is physically expected that the total integrated slope variance, and hence altimeter backscatter, will be subject to change with U_{10}, but also with a changing directional long wave field that is potentially uncoupled from the wind. The quasi-optical prediction of Eq. (5) and a two-scale surface model where $mss'_{\text{Ka}} = mss_l + mss_h$ [see Eq. (7)] provide a simple framework to investigate the issue. However, obtaining comprehensive mss_l datasets is uncommon. Several recent satellite altimeter studies attempt to quantify such uncoupled long wave impacts using surrogates for mss_l such as H_s, significant slope, and wave age (Gourrion et al. 2002a,b; Hwang et al. 1998; Gommenginger et al. 2002). Present laser-derived slope measurements provide mss_l directly and for every data sample in the set.

Results of Fig. 9 show mss_l and mss'_{Ka} increasing together at any fixed U_{10}. Knowing that mss_l variation is carried within the mss'_{Ka} integral, this is direct evidence for long-wave slope control upon the radar back-

scatter, and a clear rendering of a two scale surface response [Eq. (7)] where it is primarily the overall steepness of long-wave tilting facets that increases as one heads to sea. This, rather than changes at high wavenumber, explains first-order change in mss'_{Ka} (or σ°) in Fig. 9. The mss'_h estimates of Fig. 10 provide additional support. In a mean sense, there is invariance in this short-scale slope term among inland, coastal, and open-ocean waters.

The impact of mss_l variability upon altimeter σ° is not always small. Taking for example a linear dependence between wind and mss, observed 30%–40% changes in mss'_{Ka} will lead to equivalently large altimeter-derived wind errors. Errors of this scale were inferred for the open ocean (Gourrion et al. 2002b) and elsewhere and are directly affirmed here. Similarly, the results imply that optically based field estimation of wind-dependent total mss should consider mss_l variability following work such as Hwang and Shemdin (1988).

(iii) Radar-derived slope variance estimates are explicitly linked to the model of Eq. (5) to emphasize that mss'_{Ka} and mss'_h estimates make use of σ° data under specific approximations discussed in section 2. Quantitative comparison of results in Figs. 7 and 10 to optically derived mss data remains subject to uncertainties and varied interpretation—due in part to absolute calibration issues and to the unresolved surface wave description at all scales and conditions as mentioned in section 2. There are, however, several points to be made when considering Figs. 7, 10, and 11.

First, no effective Fresnel term is invoked in deriving mss'_{Ka}, in contrast to recent radar studies (e.g., Masuko et al. 1986; Jackson et al. 1992; Vandemark et al. 1997; Walsh et al. 1998; Hesany et al. 2000). This point reinforces studies such as Chapron et al. (2000) and Plant (2002) suggesting that such a nonphysical "effective" term is unnecessary when one considers pdf peakedness and diffraction in near-nadir radar studies alongside sensor calibration limitations. As one example, Chapron et al. (2000) provides a review of recent near-nadir radar observations (Jackson et al. 1992; Walsh et al. 1998) where mss is derived via the σ° fall off with incidence angle shown in Eq. (5) to show that these efforts are likely underestimating the true mss because of neglect of slope pdf peakedness. This underestimation in turn leads to use or modification of the effective Fresnel adjustor. If one adjusts the Ku-band mss results of Jackson et al. (1992) or the nearly equivalent Ka-band results of Walsh et al. (1998, see their Fig. 11) by the proposed blanket factor of 1.2 then one finds their results agree very well with our mss'_{Ka} data shown in Fig. 7.

Second, the variation of mss'_h with sea state seen in Fig. 11 provides a qualitative picture of likely long wave–short wave interaction of relevance in several respects. Recall that mss'_h decreases for increasing long wave roughness and that this dependency only occurs for winds above about 7 m s^{-1}. Such a result is consistent with that inferred from space (see above, Elfouhaily et al. 1998) and in the laboratory (Donelan 1987). It is also consistent with prediction of short-wave suppression by enhanced breaking due to wind drift and wave current effects under increased mechanical wave energy (Chu et al. 1992). The present mss'_h estimator does not resolve the high-wavenumber subrange carrying this response but numerous efforts would suggest $70 < k < 700$ rad m^{-1}. One implication is that a multifrequency altimeter is potentially sensitive to such long-wave and short-wave dynamics. Last, note the nearly opposite behavior for mss'_{Ka} and mss'_h with respect to mss_l change at a given moderate wind speed (Figs. 9 and 11). While the total roughness $mss'_{Ka} = mss'_h + mss_l$ appears to be rising with mss_l, the high-frequency component is decreasing. Gourrion et al. (2002b) hypothesized this contrast to be a potential source for the ambiguity observed in the satellite altimeter wind inversion process at moderate to high wind speeds. This appears to be supported by the present results.

5. Summary

The field measurements provided serve to clarify and validate several ocean wave roughness observations and models commonly invoked in the study of ocean waves and radar remote sensing of ocean winds. Wave slope pdf measurements for $\lambda > 2$ m generally affirm the oft-cited results of Cox and Munk where oil was used to eliminate short-wave scales. Present results confirm a slope distribution peakedness that greatly exceeds that for a Gaussian and exhibits a wind dependence. Both features indicate the presence of nonlinear wave–wave interactions at the intermediate gravity wave scales and occurring at all wind speeds, particularly on the open seas.

The mean wind dependence of Ka-band radar σ° indicates a high level of agreement with Ku-band satellite altimeters—an expected result. Moreover, the calibrated σ° data also indicate that past nadir-view results at Ka band are biased low by 5 dB. The radar σ° data are then used to infer slope variance at higher wavenumbers, 2 cm $< \lambda < 2$ m, as defined in Eq. (7) via combination of laser and Ka-band nadir-view scatterometer data. A key observation is that of long-wave tilt effects upon the observed radar backscatter (and mss'_{Ka}) at any given wind speed. One means used to illustrate this control is partitioning of observations into inland, coastal, and open-ocean classes. A simple geometric optics scattering model, combined with a long- and short-scale surface separation appears to be adequate to identify and quantify this phenomena. While such results are not unexpected based on many studies, the clarity gained by direct measurement of mss_l over all long-wave scales, including any swell, affirms that the primary concern when addressing long wave impacts upon σ° or mss is divining variability within a spectrally integrated parameter, for example, mss_l or the mean-square accel-

eration, that is associated with intermediate gravity wave scales. The present study suggests this variability can be quite large, particularly near the coast, and therefore of some concern in exacting mss measurements and models. Use of terms derived from low-order wave spectral moments such as H_s or k_p are unlikely to provide equivalent sensitivity to the effect.

Last, initial open-ocean results of Fig. 10 suggest that the radar-deduced slope variance for the high-wavenumber subrange is relatively insensitive to the long waves, increasing solely with the logarithm of the wind. A closer look reveals that this is true only for light-to-moderate winds below U_{10} of 7 m s^{-1}. At speeds above this range, a depression in mss$'_h$ is observed as the long-wave roughness increases. While quantitative spectral isolation of the short-wave scales dictating this observation is beyond what the present data can provide, the results are consistent with several past studies.

It is hoped that the present study serves to motivate the consideration of intermediate and long-wave scale slope measurements, and their nonlinearity, in future ocean remote sensing work. In particular, the multifrequency altimeters aboard *Jason-1* and ENVISAT, the Ku-band Tropical Rainfall Measuring Mission satellite, and developments involving GPS bistatic scattering and ocean salinity measurements. In all cases, the sensors are sensitive to these wave scales at some level. Satellite extraction of such information may prove useful to the enhanced understanding of the role that slope variance plays in gas and momentum transfer processes. Future work with this LongEZ aircraft data intends to address covariance between momentum flux variability and the wave scales resolved here.

APPENDIX

Antenna Beamwidth Impact on Nadir-Viewing $\sigma°$

Equation (4) represents the radar equation assuming that $\sigma°$ is constant across the illuminated footprint area. Equation (5) indicates that the cross section falls off quite rapidly with near-nadir incidence angle. The radar antenna beamwidth used in this experiment spans 5.8° between its half-power points. The combination of these two features suggests the need to correct nadir-view $\sigma°$ estimates to compensate for the error due to the constant $\sigma°$ assumption. This is in contrast to the satellite altimeter where the narrow effective beamwidth is of $O(0.1°)$ and the constant $\sigma°$ assumption is certainly valid.

A correction for possible cross-section variation across the footprint is developed here using a composite scattering model (e.g., Valenzuela 1978). Recall that the instantaneous aircraft $\sigma°$ measurements are derived using the power returned from a single footprint on the surface having a diameter of about 1 m. Under a composite two-scale model this measurement reflects the rough surface scattering associated with wave scales inside that m-scale patch, but also the mean tilt of the underlying surface patch away from the nominal horizontal or normal reflection angle. All $\sigma°$ values used throughout the paper represent a 5-km along-track summation over many thousand instantaneous estimates where each estimate has a unique short scale within-footprint slope variance and a mean tilt angle ($\delta = \tan\beta$) away from normal. If one assumes that the short-scale roughness is homogeneous over the flight segment and is uncorrelated with the wave slope then one can write the segment-averaged $\sigma°$ as

$$\sigma^o(0°) = \int P(\delta) \int g^2(\theta) \sigma^o_{GO}(\theta, \delta) \, d\theta \, d\delta. \quad \text{(A1)}$$

Here the antenna pattern incidence angle variation is given as $g(\theta)$, the slope probability density function is $P(\delta)$, and $\sigma°_{GO}$ (θ, δ) represents the geometrical optics cross section approximation as given by Eq. (5). An important distinction, however, is that the slope variance for this within-patch contribution is given by the short-scale component, mss$'_h$. The equation is given only for the 1D in-plane tilt case as this is adequate for the task at hand.

This equation will revert to the narrow antenna beam (e.g., satellite) result as the beamwidth tends to 0. In the flat surface limit where all tilt angles are zero this equation would depend only upon the convolution of the antenna pattern and cross-section functions. In this case the averaged $\sigma°(\theta = 0°)$ obtained using antenna beamwidths of 1–10 would fall increasingly below the true infinitely narrow beam result as the beamwidth widened.

However, the opposite effect occurs in the real-world case where the large-scale tilts become nonzero. In this case the mean reflection angle is often away from the normal specular-point direction. Now the diffuse surface scattering pattern associated with the short-scale waves is tilted away from the nominal antenna view angle θ_o. The result is that the illumination pattern is now integrated about a shifted form of the cross section [$\sigma°_{GO}$ (θ')] where the facet reflection angle is $\theta' = \theta + \delta$.

Evaluation of Eq. (A1) for varied beamwidths is performed through a Monte Carlo simulation over the tilt pdf and by assuming a Gaussian antenna pattern, shown to be in good agreement with the antennae used in the field work. Under the composite model, we assume a
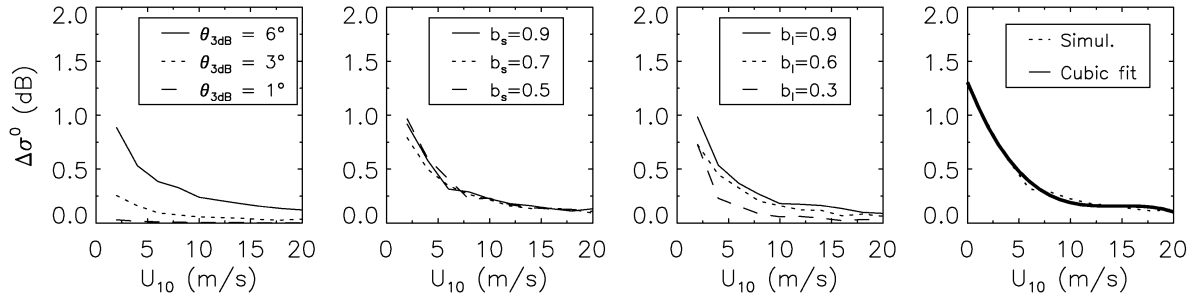
FIG. A1. Results of the $\Delta\sigma°(U_{10})$ numerical simulation. First panel: sensitivity to beamwidth change; middle panels: the sensitivity to change in the short- and long-wave roughness imposed in the two-scale simulation, respectively; final panel: $\Delta\sigma°(U_{10})$ for the case of this experiment's data, where the 3-dB beamwidth is 5.8°, along with a cubic fit approximating the simulated results.

mean wind dependence for both short- and long-wave slopes as given by Eqs. (8) and (11). The long-wave tilt values for a given run are obtained through N random draws over a slightly non-Gaussian slope pdf that supports variable levels of kurtosis to evaluate results over limits consistent with those in Fig. 5b. Results are computed as the ratio $[\Delta\sigma°(U)]$ between $\sigma°$ obtained for a given beamwidth antenna to that of an infinitely narrow beam system.

The cross-section correction limits mentioned above are readily obtained. For the case of no-tilt field, a maximum negative bias of -0.05 dB from the narrow-beam limit can be found for the case of moderate wind speeds and a beamwidth of 6. This decreases in magnitude as the wind (and hence mss'_h) decreases. Obviously this effect is small. When the tilted slope term is added, Eq. (5) is obtained for the narrow-beam limit. But a significant positive bias is found when the tilted surface is imposed and the beamwidth is increased. Figure A1 provides simulation results using this two-scale approach with 4000 realizations for any given wind speed. It is seen that $\sigma°$ is overestimated for all cases where the antenna beam width exceeds about 1° but errors are more pronounced as the width exceeds 3°. For the aircraft's 5.8° configuration the overestimate exceeds 1 dB at light winds and lessens to below 0.2 dB at the highest winds.

Bias sensitivity to various second-order factors appears to be limited. These factors include the aircraft motion, long-wave kurtosis, number of realizations in the simulation, and the extent of slope variance carried in the surface two-scale model. Scaling factors attenuating the tilting (b_L) and within-patch (b_S) slope variances are used to evaluate this last issue. The middle panels of Fig. A1 demonstrate that the effect of reducing short-wave variance is almost negligible as long as at least one-half of the mss'_h is considered. Greatly reducing the long-wave tilting lowers the error but only by about 0.2 dB. The same level of effect is seen if one completely removes the aircraft motion. Raising the long-wave kurtosis from a 1D Gaussian level of 3 to observed levels of 4–4.5 has negligible impact. The final form of the correction used in section 3 (Fig. 6)

is based on the presented cubic fit through the simulated $\sigma°$ bias results, given in decibels, and applied as

$$\sigma°(0°, U) = \langle\sigma°_{ac}(0°, U)\rangle - \Delta\sigma°(U), \qquad \text{(A2)}$$

where $\langle\sigma°_{ac}(0°, U)\rangle$ is the flight segment averaged $\sigma°$ result without this correction. The correction magnitudes are small and their estimation with this model is obviously a first-order approximation. However, they are provided as a further step in providing accurate calibration of nadir-view $\sigma°$.

REFERENCES

Apel, J. R., 1994: An improved model of the ocean surface-wave vector spectrum and its effects on radar backscatter. *J. Geophys. Res.,* **99,** 16 269–16 291.

Banner, M. L., 1990: Equilibrium spectra of wind waves. *J. Phys. Oceanogr.,* **20,** 966–984.

——, I. S. F. Jones, and J. C. Trinder, 1989: Wavenumber spectra of short gravity-waves. *J. Fluid Mech.,* **198,** 321–344.

Barrick, J., 1968a: A new model for sea clutter. *IEEE Trans. Antennas Propag.,* **16,** 217–223.

——, 1968b: Rough surface scattering based on the specular point theory. *IEEE Trans. Antennas Propag.,* **16,** 449–454.

——, 1974: Wind dependence of quasi-specular microwave sea scatter. *IEEE Trans. Antennas Propag.,* **22,** 135–136.

Bass, F., M. Fuks, A. Kalmykov, I. Ostrovsky, and A. Rosenberg, 1968: Very high frequency radiowave scattering by a disturbed sea surface. 2. Scattering from an actual sea surface. *IEEE Trans. Antennas Propag.,* **16,** 560–568.

Chapron, B., and D. Vandemark, 1996: Analysis of microwave radar cross section at low incidence. *The Air–Sea Interface: Radio and Acoustic Sensing, Turbulence and Wave Dynamics,* M. Donelan et al., Eds., Vol. 127, The University of Toronto Press, 128–132.

——, V. Kerbaol, D. Vandemark, and T. Elfouhaily, 2000: Importance of peakedness in sea surface slope measurements and applications. *J. Geophys. Res.,* **105,** 17 195–17 202.

Chen, W., M. L. Banner, E. J. Walsh, J. B. Jensen, and S. H. Lee, 2001: The southern ocean waves experiment. Part II: Sea surface response to wind speed and wind stress variations. *J. Phys. Oceanogr.,* **31,** 174–198.

Chu, J. S., S. R. Long, and O. M. Phillips, 1992: Measurements of the interaction of wave groups with shorter wind-generated waves. *J. Fluid Mech.,* **245,** 191–210.

Cox, C., and W. Munk, 1956: Slopes of the sea surface deduced from photographs of sun glitter. *Bull. Scripps Inst. Oceanogr.,* **6,** 401–488.

Donelan, M. A., 1974: Generalized profiles of wind speed, temperature and humidity. *17th Conf. on Great Lakes Research,* Ann

Arbor, MI, International Association of Great Lakes Research, 369–388.

——, 1987: The effect of swell on the growth of wind waves. *APL Tech. Dig.,* **8,** 18–23.

Dyer, A., 1974: A review of flux-profile relationships. *Bound.-Layer Meteor.,* **7,** 363–372.

Elfouhaily, T., B. Chapron, K. Katsaros, and D. Vandemark, 1997: A unified directional spectrum for long and short wind-driven waves. *J. Geophys. Res.,* **102,** 15 781–15 796.

——, D. Vandemark, J. Gourrion, and B. Capron, 1998: Estimation of wind stress using dual-frequency Topex data. *J. Geophys. Res.,* **103,** 25 101–25 108.

Fairall, C. W., E. F. Bradley, D. P. Rogers, J. B. Edson, and G. S. Young, 1996: Bulk parameterization of air–sea fluxes for Tropical Ocean Global Atmosphere Coupled Ocean Atmosphere Response Experiment. *J. Geophys. Res.,* **101,** 3747–3764.

French, J., G. Crescenti, T. Crawford, and E. J. Dumas, 2000: Longez (N3R) participation in the 1999 Shoaling Waves Experiment (SHOWEX). NOAA Data Rep. OAR ARL-20, 51 pp.

Glazman, R. E., and A. Greysukh, 1993: Satellite altimeter measurements of surface wind. *J. Geophys. Res.,* **98,** 2475–2483.

Gommenginger, C. P., M. A. Srokosz, P. G. Challenor, and P. D. Cotton, 2002: Development and validation of altimeter wind speed algorithms using an extended collocated buoy/Topex dataset. *IEEE Trans. Geosci. Remote Sens.,* **40,** 251–260.

Gotwols, B. L., and D. R. Thompson, 1994: Ocean microwave backscatter distributions. *J. Geophys. Res.,* **99,** 9741–9750.

Gourrion, J., D. Vandemark, S. Bailey, and B. Chapron, 2002a: Investigation of C-band altimeter cross section dependence on wind speed and sea state. *Can. J. Remote Sens.,* **28,** 484–489.

——, ——, ——, ——, G. P. Gommenginger, P. G. Challenor, and M. A. Srokosz, 2002b: A two-parameter wind speed algorithm for Ku-band altimeters. *J. Atmos. Oceanic Technol.,* **19,** 2030–2048.

Graber, H. C., E. A. Terray, M. A. Donelan, W. M. Drennan, and J. C. Van Leer, 2000: ASIS—A new air–sea interaction spar buoy: Design and performance at sea. *J. Atmos. Oceanic Technol.,* **17,** 708–720.

Hesany, V., W. J. Plant, and W. C. Keller, 2000: The normalized radar cross section of the sea at 10 degrees incidence. *IEEE Trans. Geosci. Remote Sens.,* **38,** 64–72.

Hwang, P. A., and O. H. Shemdin, 1988: The dependence of sea-surface slope on atmospheric stability and swell conditions. *J. Geophys. Res.,* **93,** 13 903–13 912.

——, S. Atakturk, M. A. Sletten, and D. B. Trizna, 1996: A study of the wavenumber spectra of short water waves in the ocean. *J. Phys. Oceanogr.,* **26,** 1266–1285.

——, W. J. Teague, G. A. Jacobs, and D. W. Wang, 1998: A statistical comparison of wind speed, wave height, and wave period derived from satellite altimeters and ocean buoys in the Gulf of Mexico region. *J. Geophys. Res.,* **103,** 10 451–10 468.

Jackson, F. C., W. T. Walton, D. E. Hines, B. A. Walter, and C. Y. Peng, 1992: Sea-surface mean-square slope from Ku-band backscatter data. *J. Geophys. Res.,* **97,** 11 411–11 427.

Liu, Y., X. H. Yan, W. T. Liu, and P. A. Hwang, 1997: The probability density function of ocean surface slopes and its effects on radar backscatter. *J. Phys. Oceanogr.,* **27,** 782–797.

Longuet-Higgins, M. S., 1963: The effects of non-linearities on the statistical distribution in the theory of sea waves. *J. Fluid Mech.,* **17,** 459–480.

——, 1982: On the skewness of sea surface slopes. *J. Phys. Oceanogr.,* **12,** 1283–1291.

Mahrt, L., D. Vickers, J. L. Sun, T. L. Crawford, G. Crescenti, and P. Frederickson, 2001: Surface stress in offshore flow and quasi-frictional decoupling. *J. Geophys. Res.,* **106,** 20 629–20 639.

Masuko, H., K. I. Okamoto, M. Shimada, and S. Niwa, 1986: Measurement of microwave backscattering signatures of the ocean surface using X-band and Ka-band airborne scatterometers. *J. Geophys. Res.,* **91,** 3065–3083.

Melville, W. K., and P. Matusov, 2002: Distribution of breaking waves at the ocean surface. *Nature,* **417,** 58–63.

——, R. H. Stewart, W. C. Keller, J. A. Kong, D. V. Arnold, A. T. Jessup, M. R. Loewen, and A. M. Slinn, 1991: Measurements of electromagnetic bias in radar altimetry. *J. Geophys. Res.,* **96,** 4915–4924.

Paulson, C. A., 1970: The mathematical representation of wind speed and temperature profiles in the unstable atmospheric surface layer. *J. Appl. Meteor.,* **9,** 857–861.

Phillips, O. M., 1977: *The Dynamics of the Upper Ocean.* 2d ed. Cambridge University Press, 336 pp.

Plant, W. J., 2002: A stochastic, multiscale model of microwave backscatter from the ocean. *J. Geophys. Res.,* **107,** 3120, doi:10.1029/2000JC000909.

Shaw, J. A., and J. H. Churnside, 1997: Scanning-laser glint measurements of sea-surface slope statistics. *Appl. Opt.,* **36,** 4202–4213.

Stogryn, A., 1997: Equations for the permittivity of sea water. Gencorp Aerojet Tech. Rep.

Sun, J. L., D. Vandemark, L. Mahrt, D. Vickers, T. Crawford, and C. Vogel, 2001: Momentum transfer over the coastal zone. *J. Geophys. Res.,* **106,** 12 437–12 448.

Sverdup, H., and W. Munk, 1947: Wind, sea, and swell: Theory of relations for forecasting. U.S. Hydrographic Office Tech. Rep. 1, 44 pp.

Tatarskii, V. I., 2003: Multi-Gaussian representation for the Cox–Munk distribution of slopes for wind-driven waves. *J. Atmos. Oceanic Technol.,* **20,** 1697–1705.

Valenzuela, G. R., 1978: Theories for the interaction of electromagnetic and oceanic waves: A review. *Bound.-Layer Meteor.,* **13,** 61–85.

Vandemark, D., J. B. Edson, and B. Chapron, 1997: Altimeter estimation of sea surface wind stress for light to moderate winds. *J. Atmos. Oceanic Technol.,* **14,** 716–722.

——, T. Crawford, R. Dobosy, T. Elfouhaily, and B. Chapron, 1999: Sea surface slope statistics from a low-altitude aircraft. *Int. Geosci. Remote Sens. Symp.,* Vol. 2, Hamburg, Germany, IEEE, 381–383.

——, P. D. Mourad, S. A. Bailey, T. L. Crawford, C. A. Vogel, J. Sun, and B. Chapron, 2001: Measured changes in ocean surface roughness due to atmospheric boundary layer rolls. *J. Geophys. Res.,* **106,** 4639–4654.

Vickers, D., L. Mahrt, J. L. Sun, and T. Crawford, 2001: Structure of offshore flow. *Mon. Wea. Rev.,* **129,** 1251–1258.

Walsh, E. J., D. C. Vandemark, C. A. Friehe, S. P. Burns, D. Khelif, R. N. Swift, and J. F. Scott, 1998: Measuring sea surface mean square slope with a 36-GHz scanning radar altimeter. *J. Geophys. Res.,* **103,** 12 587–12 601.